

Macroscale superlubricity enabled by rationally designed MoS₂-based superlattice films

Siming Ren

Ningbo Institute of Materials Technology and Engineering, Chinese Academy of Sciences

Mingjun Cui

Ningbo University

Ashlie Martini

University of California - Merced

Yanbin Shi

Ningbo Institute of Materials Technology and Engineering, Chinese Academy of Sciences

Haixin Wang

Ningbo Institute of Materials Technology and Engineering, Chinese Academy of Sciences

Jibin Pu

Ningbo Institute of Materials Technology and Engineering, Chinese Academy of Sciences

Qunyang Li

Tsinghua University <https://orcid.org/0000-0002-6865-3863>

Liping Wang (✉ wangliping@nimte.ac.cn)

Ningbo Institute of Materials Technology and Engineering, Chinese Academy of Sciences

Article

Keywords:

Posted Date: February 22nd, 2022

DOI: <https://doi.org/10.21203/rs.3.rs-1356825/v1>

License:   This work is licensed under a Creative Commons Attribution 4.0 International License.

[Read Full License](#)

Abstract

Although superlubricity is highly desirable for many engineering applications, its implementation has so far been seriously restricted due to limitations in contact size, environmental adaptability and life time. By designing superlattice films with alternating molybdenum disulfide (MoS_2) and tungsten carbide (WC) layers, we show that long-term macroscale superlubricity (friction coefficient of 0.006) in low vacuum ($\sim 10^{-3}$ Pa) after a short running-in period in air. Such unusual behavior is enabled when the fine structure of the bilayer unit is rationally controlled to yield incommensurate contacts between MoS_2 and metal oxides nanoparticles produced spontaneously during tribological sliding. Our analysis indicates that the WC phase is critical for superlubricity by helping stiffen the film, facilitate preferential growth of crystalline MoS_2 along (002) plane parallel to substrate, and produce lubricous nanoparticles. We further demonstrate the superlattice design is generally applicable for MoS_2 /ceramics materials to achieve long life-time macroscale superlubricity with easy self-rejuvenation capability.

Introduction

Friction and wear are one of the primary mechanisms for energy dissipation and material failure in mechanical systems with moving parts¹. To minimize their adverse effects, various strategies have been proposed and adopted in history², among which applying solid lubricants is one of the most effective means. Molybdenum disulfide (MoS_2), as a well-known solid lubricant, has been extensively used to reduce friction and wear owing to its unique lamellar structure with easy-shear interfaces between atomic layers^{3,4}. However, as the dangling bonds at the edges of MoS_2 planes are highly reactive in air or in low vacuum, good lubrication performance (friction coefficient less than 0.05) is typically restricted to high-vacuum conditions⁵. Particularly, when MoS_2 films with good crystallinity are in-situ prepared and tested in ultra-high vacuum, superlubricity (friction coefficient on the order of 10^{-3}) can be achieved for a limited time period⁶⁻⁸. Encouraged by the good promise, researchers have tried doping the MoS_2 -based films with metals, nonmetals and compounds to help improve their endurance and tribological performance⁹⁻¹³. However, fabricating thick MoS_2 -based films with good crystallinity and wear resistance is still technically challenging.

Besides MoS_2 , great efforts have been dedicated to achieve superlubric sliding by using other layer-structured materials¹⁴⁻²². A breakthrough in microscale superlubricity was made with a graphite flake sliding over a graphite mesa reaching a contact area up to $10 \mu\text{m} \times 10 \mu\text{m}$ ¹⁷. Further strategies by dividing macroscale sliding interfaces into multiple microscale incommensurate contact sites appear to be a feasible route towards macroscale superlubricity. For example, macroscale superlubricity could be achieved by using graphene wrapped nano-diamonds sliding against a diamond-like carbon coated surface, or by constructing 2D layered heterostructures on textured substrates^{18,19}. Despite the limited success, achieving superlubricity typically requires a strict control of surface morphology or introducing

additives at the sliding interface. More importantly, once the superlubric sliding interface is damaged by excessive loads or when the additives are exhausted, superlubricity breaks down inevitably.

As discussed above, constructing multi-contact junctions between layer-structured materials and other crystalline materials is an effective way for achieving macroscale superlubricity²³⁻²⁵. Therefore, if one can sandwich a hard phase polycrystalline material between ordered MoS₂ layers to build a superlattice structure, the MoS₂ can continue to replenish itself during the tribological process, which may lead to a long-term superlubricity. Unfortunately, until now, the MoS₂ phase in most MoS₂-based multilayer films typically exhibits a poor crystallinity²⁶⁻²⁸, which prohibits superlubric sliding or restricts the superlubric state in a short-term period. In this work, a novel MoS₂/WC superlattice film was fabricated with precisely designed thickness of constituent layers. The superlattice film could achieve long-term and robust superlubricity in vacuum after undergoing a short running-in in air. Assisted by detailed sliding interface analysis and comparative experiments, we have shown that the thin WC sublayer played a critical and unique role for achieving excellent performance: It served as a rigid backing substrate to reduce film deformation, facilitated preferential growth of crystalline MoS₂ and contributed to the formation of lubricating metal oxide nanoparticles. Finally, we also demonstrated that such superlattice structure could be easily extended to other MoS₂/ceramic systems to achieve robust macroscale superlubricity.

Results

Preparation and characterization of films. The MoS₂/WC superlattice films were fabricated on 304 stainless steel and silicon wafer using a closed-field unbalanced magnetron sputtering system, where one Ti target, four MoS₂ targets and one WC target were sequentially arranged in the chamber (Fig. 1a). The structure of the resultant MoS₂/WC film is schematically shown in Fig. 1b, which consists of a Ti adhesion layer, an intermediate Ti/MoS₂/WC layer and an alternating MoS₂/WC multilayer. By choosing appropriate target current (see more details in Supplementary Table 1, Figs. 1 and 2), we could precisely control the thickness of each individual sublayer within the MoS₂/WC bilayer unit. According to the transmission electron microscopy (TEM) images, the MoS₂ (light) and WC (dark) layers are alternated to form a ripple-like structure (inset in Fig. 1b), and the corresponding thickness of the MoS₂ and WC layers in individual bilayer are ~6.5 nm and ~1.6 nm, respectively (Supplementary Fig. 3). The MoS₂ in the superlattice film grows preferentially along the (002) crystal plane parallel to the substrate, in sharp contrast to the random-oriented phase typically exhibited by pure thick MoS₂ films (Supplementary Fig. 4).

Frictional characteristics of films. To characterize the tribological performance of the MoS₂/WC superlattice film, we carried out comparative friction experiments by sliding GCr15 steel balls against superlattice film as well as sputtered pure MoS₂ film in linear reciprocating mode. The experiments were conducted in vacuum, humid air and alternating vacuum-air to explore the environmental adaptability. As

indicated in Fig. 1c and Supplementary Fig. 5, under humid air condition, the pure MoS₂ film is worn out after a short period (~5700 cycles) and its friction coefficient exceeds the limit range of the tribometer (> 0.5). In contrast, the MoS₂/WC superlattice film achieves a low friction coefficient of 0.04~0.05 after a short running-in stage and it remains at the low friction level throughout the test. In addition to the marked improvement in tribological performance in humid air, the superlattice film also excels in vacuum condition. As shown in Fig. 1c, although pure MoS₂ is known to perform much better in vacuum than in air, its friction coefficient is still relatively high (ranging from 0.03 to 0.065) and fluctuates noticeably. But the MoS₂/WC superlattice film exhibits a low and stable friction coefficient (ranging from 0.01 to 0.02) throughout the test. By comparing it with other state-of-the-art MoS₂-based materials, one can see the MoS₂/WC superlattice film outperforms its peers either in air or in vacuum (Fig. 1d, Supplementary Table 2).

Apart from the excellent properties in vacuum and air, the most striking feature of the MoS₂/WC superlattice film lies in its performance in alternating vacuum-air environment. Figure 1e shows the variation of friction coefficient measured on the superlattice film when the experimental chamber was periodically switched between vacuum and air conditions. Similar to the behavior shown in Fig. 1c, the value of friction coefficient also alternates between high and low corresponding to the periodical change in environment. However, in this alternating mode, one can see that the friction coefficient under vacuum condition can reach an appreciably lower value. For example, the friction coefficient in vacuum is smaller than 0.01 after only one environmental cycle and it decreases progressively reaching a steady value of 0.006, which signifies stable macroscale superlubricity.

Environmentally adaptive behavior of superlattice films. To understand the improved performance of the MoS₂/WC superlattice film under different environments, we examined the wear tracks on the films and the wear scars on the steel balls using Raman spectroscopy and TEM. For the sample pair tested in vacuum, the wear track appears to be smooth and burnished without formation of new phases (Fig. 2a). The width (~140 μm) and depth (~0.6 μm) of the wear track are significantly smaller than those of pure sputtered MoS₂ film with a width of ~210 μm and a depth of ~2.2 μm under the same test conditions (Supplementary Fig. 6). According to the Raman spectra shown in Fig. 2b, MoS₂ is abundant both in the wear track and the wear scar as evident by the pronounced peaks at around 375 cm⁻¹ and 410 cm⁻¹ corresponding to the E_{2g}¹ and A_{1g} modes of MoS₂ crystal^{29,30}. This suggests that the MoS₂ sublayer with preferred (002) crystal plane in the superlattice film has outstanding stability and wear resistance, in contrast to the poor crystallinity and the loose structure exhibited by the pure MoS₂ film (Supplementary Fig. 7). Meanwhile, the WC sublayer serving as a load supporting layer also provided a hard substrate for MoS₂ to reduce its deformation and enhance wear resistance (Supplementary Fig. 8), as evidenced by less formation of wear debris along the periphery of wear track (region II in Fig. 2a). In addition to the characteristic peaks of MoS₂, strong signals of WS₂ (515 cm⁻¹)³¹ and amorphous carbon (a-C, 1345 and

1595 cm^{-1} corresponding to the D and G peaks)³² were also detected from the tribofilm (region III in Fig. 2a), indicating that the WC phase at the sliding interface was transformed into WS_2 and a-C under the high contact pressure and shear. High resolution TEM (HRTEM) images (Fig. 2c and Supplementary Fig. 9) demonstrate that the tribofilm is dominated by MoS_2 with a significant fraction of a-C phase and sparsely distributed WS_2 nanocrystals. The transferred film with cross-linked MoS_2 /a-C structure could interact with MoS_2 of the substrate to form an incommensurate interface, thereby minimizing the sliding resistance. However, as a-C is composed of mixed sp^3/sp^2 bonded carbon, although some of the carbon atoms are passivated by sulfur (Supplementary Fig. 10), carbon dangling bonds are still expected to exist, prohibiting full superlubricity^{33,34}.

In contrast to the case in vacuum, for the friction pair tested in air, the periphery of the worn surface is covered with a significant amount of wear debris after 90,000 sliding cycles (Fig. 2d). Raman analysis of the wear debris (Fig. 2e) reveals three noticeable features including MoS_2 , metal oxides (MeO_x , e.g. WO_3/MoO_x)³⁵ and a-C, which suggests that the WC phase has been converted to WO_3 and a-C via tribochemical reactions. Meanwhile, Raman and XPS spectra indicate that the wear track and the tribofilm are dominated by MoS_2 and $\text{MoS}_2/\text{MeO}_x$, respectively (Fig. 2e and Supplementary Fig. 10). In this scenario, the formed a-C that is not conducive to low friction has been pushed to the outside of the sliding interface, explaining why the carbon-containing wear debris is enriched around the wear track. Further HRTEM image of the tribofilm (Fig. 2f) shows that the tribofilm is mainly composed of MoS_2 matrix and randomly distributed MeO_x nanoparticles. Therefore, sliding in air was likely to occur between MoS_2 and MoS_2 with intercalated MeO_x nanoparticles, as schematically shown in Fig. 2f. The nanoscale incommensurate $\text{MoS}_2/\text{MeO}_x$ interface helped minimize direct $\text{MoS}_2/\text{MoS}_2$ contact and could also provide possible rolling contacts, both of which were beneficial for lowering the sliding resistance^{36,37}, as suggested by the results shown in Fig. 1d. However, according to TEM images, the MoS_2 in the transferred tribofilm was primarily amorphous and almost no large-scale ordered lamellar structure could be found (Supplementary Fig. 11). This loss of crystallinity, possibly caused by the aggressive oxidation reactions during friction test in air, prohibited the sliding interface from entering a lower friction regime²².

Robust superlubricity mechanisms of superlattice film. To explore the underlying mechanism for the observed superlubricity in alternating vacuum-air environment, we repeated the friction experiment and then interrupted it during the vacuum stage of the third alternating period to examine the interface state (Fig. 3a). As shown in Fig. 3b, optical image indicates that a compact tribofilm has already been formed after the system underwent two test periods. The corresponding Raman intensity maps suggest that the tribofilm mainly consists of MoS_2 and MeO_x , where the MeO_x is surrounded by MoS_2 matrix (Fig. 3b and Supplementary Fig. 12). In the cross-sectional TEM images of the tribofilm (Fig. 3c), a large number of black spots and lines can be observed, which are identified to be MeO_x nanoparticles and MoS_2 flakes respectively based on their atomic spacings^{38,39}. More importantly, the MeO_x nanoparticles in the

superlubricous state are surrounded by thin MoS₂ flakes with ordered structures, in sharp contrast to the amorphous structure found in the tribofilm formed in air environment (Fig. 2f). It is possible that, under shear stress of macroscale friction, highly ordered MoS₂ is readily transferred from the substrate film to the counterpart ball or the MeO_x nanoparticles. Therefore, the superlubricity interface might be a result of sliding/rolling of MoS₂-wrapped MeO_x nanoparticles that are sandwiched between highly ordered MoS₂ flakes, as schematically shown in Fig. 3d. This is somewhat similar to the superlubricity mechanism reported by Sumant et al.^{18,19}; however, in our system, nanoparticles were formed spontaneously through reactions between the film components and the aggressive species during the running-in stage without adding nanoparticles or 2D materials separately. Noticeably, we further confirmed that water was the key factor to promote the formation of MeO_x nanoparticles, rather than oxygen (see more details in Supplementary Fig. 13).

Discussion

As mentioned above, the WC layer in the superlattice film plays an important role in achieving superlubricity. First, it helps minimize the deformation and wear of MoS₂ by increasing the film hardness and facilitates the preferential growth of MoS₂ with (002) plane orientation. In the meantime, WC also tribochemically reacts with atmospheric species to form abundant MeO_x nanoparticles, thereby dividing the macroscopic contact area into many incommensurate nano-contact zones to ensure robust superlubricity. To optimize the aforementioned effects, we found that an appropriate thickness modulation ratio of the MoS₂/WC bilayer unit was very critical. For example, when the WC target current during growth was lowered to 0.4~0.6 A, the resultant WC phase became non-continuous and the film would lose the multilayer structure and turn into a composite structure (left in Fig. 4a). The isolated WC phase could not support the load effectively, resulting in poor mechanical properties (Supplementary Fig. 1) and worse tribological performance (Fig. 4b). However, if the thickness of the WC layer became too thick under a higher target current (right panel of Fig. 4a), the resultant film would become brittle and easily get delaminated due to large mismatch in mechanical properties between MoS₂ layer and WC layer. More importantly, if the WC layer thickness was too thick, sliding started to occur between WC-WC contacts, leading to a premature failure of the film (Fig. 4b).

Based on the analysis of alternating air-vacuum test results, the main contribution of the air stage is to generate the MeO_x nanoparticles needed in the superlubricous stage in vacuum. Therefore, we speculate that as long as a stable MoS₂/MeO_x sliding interface can be established, the air stage is not necessarily to be as long as the vacuum stage. To validate our hypothesis, we conducted additional alternating air-vacuum friction test but reducing the air stage to 3,000 sliding cycles while prolonging the vacuum stage to 47,000 sliding cycles. As confirmed by the results shown in Fig. 4c, the friction coefficient for all the vacuum stages is in the superlubric regime and its value in vacuum decreases progressively with each period, suggesting that a short sliding period in air indeed can ensure stable superlubricity for a long period in vacuum. The corresponding specific wear rate of the superlattice film is as low as 4.0×10^{-8}

$\text{mm}^3 \text{N}^{-1} \text{m}^{-1}$ after 200,000 sliding cycles (Fig. 4d). Note that the film wear mainly occurs at the first running-in stage in air (Supplementary Fig. 14). Once the robust $\text{MoS}_2/\text{MeO}_x$ incommensurate multi-contact points are established at the sliding interface after 3,000-cycle in air, the specific wear rate of the superlattice film will reach the ultralow level on the order of $10^{-9} \text{mm}^3 \text{N}^{-1} \text{m}^{-1}$ for the subsequent 197,000 sliding cycles. Further experiment indicated that the $\text{MoS}_2/\text{MeO}_x$ interface formed during a short 3000-cycle air period could effectively sustain robust superlubricity for more than 80,000 sliding cycles in vacuum (Supplementary Fig. 15). Amazingly, macroscale superlubricity was also achieved on another MoS_2 /carbide superlattice film, i.e., MoS_2/SiC system, where the thickness of the MoS_2 and SiC layers in one bilayer was $\sim 6.5 \text{ nm}$ and $\sim 2.0 \text{ nm}$, respectively (Fig. 4e). The friction coefficient of the MoS_2/SiC superlattice film is below 0.01 during the vacuum stage after one period due to formation of a $\text{MoS}_2/\text{MoO}_x$ sliding interface in the air stage (Fig. 4f, g). This demonstration shows that rational design of superlattice structures opens a new pathway for traditional solid lubricating films to achieve superlubricity for long-term applications.

In summary, a superlattice film consisting of alternating MoS_2 and WC sublayers has been designed to achieve robust long-term macroscale superlubricity in vacuum after a short running-in in air. This unusual property is possible only when the fine structure of the bilayer unit is precisely controlled such that the WC phase can synergetically increase film stiffness, induce preferential growth of crystalline MoS_2 and form lubricous metal oxide nanoparticles. Therefore, a macroscopic contact area is divided into numerous incommensurate nano-contact zones during a very short atmospheric test to ensure robust superlubricity with a history-long of more than 80,000 sliding cycles and an ultralow level of specific wear rate on the order of $10^{-9} \text{mm}^3 \text{N}^{-1} \text{m}^{-1}$. Such a unique design can be easily extended to other layer-structured materials/ceramics structures to achieve macroscale superlubricity. The general applicability of the superlattice design and the long life time of the easily self-rejuvenating films will enable macroscale superlubricity with realistic engineering significance.

Methods

Materials preparation. All the MoS_2/WC films were prepared on steel substrates and silicon wafers simultaneously using a closed field unbalanced magnetron sputtering system (Teer, CF-800, UK). Six targets sputtered with direct current power were mounted on the biaxial rotating sample holder in the center of vacuum chamber, where the targets were arranged counterclockwise in order of one Ti target (99.99% in purity), four MoS_2 targets (99.99% in purity) and one WC target (99.99% in purity), as schematically shown in Fig. 1a. Prior to the film deposition, all substrates were ultrasonically cleaned successively in acetone and alcohol for 20 min, and then etched by argon plasma with a substrate pulsed bias of -500 V for 30 min to remove the surface contaminations. Subsequently, a thin Ti interlayer was deposited with a target current of 3.0 A to enhance the adhesion strength between film and substrate. After the Ti interlayer was deposited for 20 min, the target current of Ti was decreased gradually to zero while the target currents of MoS_2 and WC were progressively increased to the target

current. The final step was deposition of the bulk MoS₂/WC films, where the target current of MoS₂ was maintained at 1.6 A, and MoS₂/WC films with different modulation ratios could be prepared by adjusting the target current of WC (WC: 0.4, 0.6, 0.8, and 1.0 A). Detailed parameters for the deposition of the bulk MoS₂/WC films are given in Supplementary Table 1. Each film deposition process started at a background vacuum less than 5×10^{-5} Pa, and the film deposition was conducted at a substrate pulsed bias of -50 V and a Ar working gas (99.99% in purity) of 16 sccm. The rotation rate of specimen holder was controlled at 2 rpm to obtain a nano-multilayer structure. For the deposition of pure MoS₂ film, the WC target was protected by aluminum foil and its current was modulated to zero. For the MoS₂/SiC film, the WC target was replaced by the SiC target. The corresponding target currents of MoS₂ and SiC were maintained at 1.6 A and 0.8 A, respectively. The other deposition parameters of pure MoS₂ and MoS₂/SiC films are consistent with the above-mentioned.

Friction and wear tests. All the friction tests were carried out in a ball-on-disc reciprocating sliding tribometer (CSM, Tribo-S-D-0000, Switzerland), and the gas environment in the chamber was controlled. The films coated steel substrates were driven to slide against the counterpart steel ball ($\Phi 6$ mm, GCr15, Ra \approx 20 nm, Hardness: 6.1 GPa) at the room temperature (25 ± 2 °C) with an amplitude of 5 mm, a frequency of 5 Hz (maximum line speed of 50 mm s⁻¹), a normal load of 5 N (maximum Hertz contact pressure of 1.0 GPa). The friction tests were performed in four environments: vacuum (less than 5.0×10^{-3} Pa), air (RH $40 \pm 2\%$), an alternate vacuum-air environment and an alternate vacuum-oxygen gas environment. The relative humidity of the chamber in the tribometer was controlled with a humidifier. A dry oxygen environment was produced by purging the oxygen gas into the chamber and the chamber pressure maintained at around 5.0×10^3 Pa for 10 min without any significant change in pressure. The tribometer was automatically calibrated before each sliding test, and all the friction tests were repeated at least three times to ensure reproducibility of the results. Specific wear rates were based on a volumetric material loss of the flat for per load and sliding distance ($K=V/FL$), where V was the volumetric material loss measured by a surface profiler with contact mode (Alpha-step D-100), F represented the normal load (N), and L represented the total sliding distance (m).

Characterization of prepared films. Scanning electron microscope (SEM, Thermo Scientific, Verios G4 UC, USA) equipped with electron dispersive spectroscopy (EDS, Oxford X-Max 50) was used to characterize the cross-sectional morphologies and the elemental composition of the as-prepared films. The surface morphologies and roughness of the as-prepared films were characterized by scanning probe microscope (SPM, Bruker, Dimension Icon, Germany) using a commercial silicon probe in tapping mode. The mechanical properties, including hardness and elastic modulus, of all the as-prepared films were evaluated by nanoindentation (MTS, NANO G200, USA) using a Berkovich diamond tip with an indentation depth of approximately 200 nm (less than 10% of film thickness) to minimize the effect of

the substrates. The structure of the as-prepared films were identified by X-ray diffraction (XRD, Bruker, D8 Discover, Germany) using Cu K α radiation and the scanning angle ranging from 5° to 90°. Transmission electron microscopy (TEM, FEI, Talos F200, USA) and high resolution TEM (HRTEM), equipped with a high-angle annular dark-field detector (HAADF) and EDS, was performed to analyze the cross-sectional morphologies, elemental distribution and microstructures of the specific lamellar specimens obtained from the as-prepared films grown on silicon wafers. The lamellar specimens used for TEM and scanning TEM (STEM) tests were prepared by a dual-beam focused ion beam (FIB, Zeiss, NEON 40EsB Crossbeam, Germany), followed by a low Ga⁺ ion-beam milling using the precision ion polishing system (PIPS). Before the process of Ga⁺ ion milling, a protection layer of Pt or carbon layer was coated on the sample surface via ion sputtered system.

Characterization of rubbing areas. The contact areas, including the film wear tracks and the ball wear scars, were imaged by an optical microscope (Zeiss, LSM 700, Germany). The bonding structure and configuration in the tribofilms, wear tracks and wear debris were detected by visible Raman spectroscopy (Renishaw, inVia-reflex, excitation $\lambda = 532$ nm). The spatial distribution and the corresponding Raman intensity of the tribofilm components were quantified spatially using image Raman spectroscopy (excitation $\lambda = 532$ nm, 1mW). The Raman scanning area was about 100 μm^2 , the step size of the scans was 4 μm , and a total of 625 points were detected. The power of the excitation laser was less than 1 mW to avoid heating effects. The amplitude of the characterized peaks of MoS₂, metal oxides as well as G peak of amorphous carbon for each Raman spectrum was determined by the instrument fitting procedure. The functional groups and surface chemical composition of the as-prepared films and tribofilms transferred on the steel ball were characterized by X-ray photoelectron spectroscopy (XPS, AXIS ULTRA DLD, Japan) using Al (mono) K α radiation source with pass energy of 160 eV. The XPS spectra were fitted using the CasaXPS software with a Shirley background.

Fourier transform infrared (FTIR) microspectroscopy (Agilent, Cary660 + 620, USA) was carried out to determine the tribofilm composition, and the wavenumber ranges from 900 to 2000 cm^{-1} . IR absorption maps were used to analyze the spatial distribution of the -OH stretching absorbance in the tribofilm, where the -OH absorption maps were generated by integrated peak area of IR absorbance from 1700 to 1580 cm^{-1} . The area of analysis was about 5.5 \times 5.5 μm^2 that is covered an area including the ball wear scar. IR maps were collected by adding 64 scans at each sample position with a spectral resolution of 4 cm^{-1} .

Similar to the preparation of lamellar specimens for the as-prepared films, FIB was used to obtain cross-sections of the tribofilm on the steel ball in different environments. The cross-sectional morphologies and microstructure of tribofilms were analyzed by TEM and HRTEM. The fast Fourier transform (FFT) patterns based on the HRTEM data were processed by the DigitalMicrograph software.

Data availability

The authors declare that all data supporting the findings of this study are available within the article and its Supplementary Information files. Source data are provided with this paper.

References

1. Holmberg, K. & Erdemir, A. Influence of tribology on global energy consumption, costs and emissions. *Friction* **5**, 263-284 (2017).
2. Dowson, D. *History of tribology* (Professional Engineering Publishing, London, 1998).
3. Li, H. et al. Superlubricity between MoS₂ Monolayers. *Adv. Mater.* **29**, 1701474 (2017).
4. Lee, C. et al. Frictional characteristics of atomically thin sheets. *Science* **328**, 76-80 (2010).
5. Vazirisereshk, M. R., Martini, A., Strubbe, D. A. & Baykara, M. Z. Solid lubrication with MoS₂: A Review. *Lubricants* **7**, 57 (2019).
6. Martin, J. M., Donnet, C., Le Mogne, T. & Epicier, T. Superlubricity of molybdenum disulphide. *Phys. Rev. B* **48**, 10583-10586 (1993).
7. Hirano, M. & Shinjo, K. Atomistic locking and friction. *Phys. Rev. B* **41**, 11837-11851 (1990).
8. Donnet, C., Martin, J. M., Le Mogne, T. & Belin, M. Super-low friction of MoS₂ coatings in various environments. *Tribol. Int.* **29**, 123-128 (1996).
9. Vellore, A. et al. Ni-doped MoS₂ dry film lubricant life. *Adv. Mater. Interfaces* **7**, 2001109 (2020).
10. Ren, S., Li, H., Cui, M., Wang, L. & Pu, J. Functional regulation of Pb-Ti/MoS₂ composite coatings for environmentally adaptive solid lubrication. *Appl. Surf. Sci.* **401**, 362-372 (2017).
11. Xu, J. et al. Growth and characteristics of self-assembled MoS₂/Mo-S-C nanoperiod multilayers for enhanced tribological performance. *Sci. Rep.* **6**, 25378 (2016).
12. Scharf, T. W., Kotula, P. G. & Prasad, S. V. Friction and wear mechanisms in MoS₂/Sb₂O₃/Au nanocomposite coatings. *Acta Mater.* **58**, 4100-4109 (2010).
13. Duan, Z. et al. MoS₂ nanocomposite films with high irradiation tolerance and self-adaptive lubrication. *ACS Appl. Mater. Interfaces* **13**, 20435-20447 (2021).
14. Hod, O., Meyer, E., Zheng, Q. & Urbakh, M. Structural superlubricity and ultralow friction across the length scales. *Nature* **563**, 485-492 (2018).

15. Zhang, S., Ma, T., Erdemir, A. & Li, Q. Tribology of two-dimensional materials: From mechanisms to modulating strategies. *Mater. Today* **26**, 67-86 (2019).
16. Zhang, R. et al. Superlubricity in centimetres-long double-walled carbon nanotubes under ambient conditions. *Nat. Nanotechnol.* **8**, 912-916 (2013).
17. Liu, Z. et al. Observation of microscale superlubricity in graphite. *Phys. Rev. Lett.* **108**, 205503 (2012).
18. Berman, D., Deshmukh, S. A., Sankaranarayanan, S. K. R. S., Erdemir, A. & Sumant, A. V. Macroscale superlubricity enabled by graphene nanoscroll formation. *Science* **348**, 1118-1122 (2015).
19. Berman, D. et al. Operando tribochemical formation of onion-like-carbon leads to macroscale superlubricity. *Nat. Commun.* **9**, 1164 (2018).
20. Kawai, S. et al. Superlubricity of graphene nanoribbons on gold surfaces. *Science* **351**, 957-961 (2016).
21. Koren, E., Lörtscher, E., Rawlings, C., Knoll, A. W. & Duerig, U. Adhesion and friction in mesoscopic graphite contacts. *Science* **348**, 679-683 (2015).
22. Li, P. et al. Toward robust macroscale superlubricity on engineering steel substrate. *Adv. Mater.* **32**, 2002039 (2020).
23. Song, Y. et al. Robust microscale superlubricity in graphite/hexagonal boron nitride layered heterojunctions. *Nat. Mater.* **17**, 894-899 (2018).
24. Liu, S. W. et al. Robust microscale superlubricity under high contact pressure enabled by graphene-coated microsphere. *Nat. Commun.* **8**, 14029 (2017).
25. Song, Y., Qu, C., Ma, M. & Zheng, Q. Structural superlubricity based on crystalline materials. *Small* **16**, e1903018 (2020).
26. Wu, Y. et al. A long-lifetime MoS₂/a-C:H nanoscale multilayer film with extremely low internal stress. *Surf. Coat. Technol.* **236**, 438-443 (2013).
27. Gao, X. et al. Constructing WS₂/MoS₂ nano-scale multilayer film and understanding its positive response to space environment. *Surf. Coat. Technol.* **353**, 8-17 (2018).
28. Yin, X., Jin, J., Chen, X., Ma, T. & Zhang, C. A new pathway for superlubricity in a multilayered MoS₂-Ag film under cryogenic environment. *Nano Lett.* **21**, 10165-10171 (2021).
29. Li, H. et al. From bulk to monolayer MoS₂: Evolution of raman scattering. *Adv. Funct. Mater.* **22**, 1385-1390 (2012).

30. Fan, X. et al. MoS₂/WS₂ nanosheet-based composite films irradiated by atomic oxygen: Implications for lubrication in space. *ACS Appl. Nano Mater.* **4**, 10307-10320 (2021).
31. Deepthi, B. et al. Mechanical and tribological properties of sputter deposited nanostructured Cr-WS₂ solid lubricant coatings. *Surf. Coat. Technol.* **205**, 1937-1946 (2010).
32. Chen, X. et al. Atomic-scale insights into the interfacial instability of superlubricity in hydrogenated amorphous carbon films. *Sci. Adv.* **6**, eaay1272 (2020).
33. Chen, X. et al. Evolution of tribo-induced interfacial nanostructures governing superlubricity in a-C:H and a-C:H:Si films. *Nat. Commun.* **8**, 1675 (2017).
34. Wang, F., Wang, L. & Xue, Q. Fluorine and sulfur co-doped amorphous carbon films to achieve ultra-low friction under high vacuum. *Carbon* **96**, 411-420 (2016).
35. Dieterle, M., Weinberg, G. & Mestl, G. Raman spectroscopy of molybdenum oxides. *Phys. Chem. Chem. Phys.* **4**, 812-821 (2002).
36. Sheehan, P. E. & Lieber, C. M. Nanotribology and nanofabrication of MoO₃ structures by atomic force microscopy. *Science* **272**, 1158-1161 (1996).
37. Liang, T., Sawyer, W. G., Perry, S. S., Sinnott, S. B. & Phillpot, S. R. First-principles determination of static potential energy surfaces for atomic friction in MoS₂ and MoO₃. *Phys. Rev. B* **77**, 104105 (2008).
38. Wang, M., Chen, Y., Gao, B. & Lei, H. Electrochromic properties of nanostructured WO₃ thin films deposited by glancing-angle magnetron sputtering. *Adv. Electron. Mater.* **5**, 1800713 (2019).
39. Chen, X. et al. Vertical 2D MoO₂/MoSe₂ core-shell nanosheet arrays as high-performance electrocatalysts for hydrogen evolution reaction. *Adv. Funct. Mater.* **26**, 8537-8544 (2016).

Declarations

Acknowledgements

We are grateful for financial support from the National Science Fund for Distinguished Young Scholars of China (Grant Nos. 51825505, 12025203), the National Natural Science Foundation of China (Grant No. 52005489), and the China Postdoctoral Science Foundation (Grant No. 2021T140685).

Author contributions

Q.L., S.R. and L.W. developed the concept, designed the experiments, and supervised the projects. H.W. and Y.S. prepared the samples. S.R. characterized structure and performed the measurements. All authors

discussed and analyzed the results. S.R., M.C., A.M., and Q.L. wrote the paper.

Competing interests

The authors declare no competing interests.

Additional information

Supplementary information The online version contains supplementary material available at

Correspondence and requests for materials should be addressed to Qunyang Li or Liping Wang.

Figures

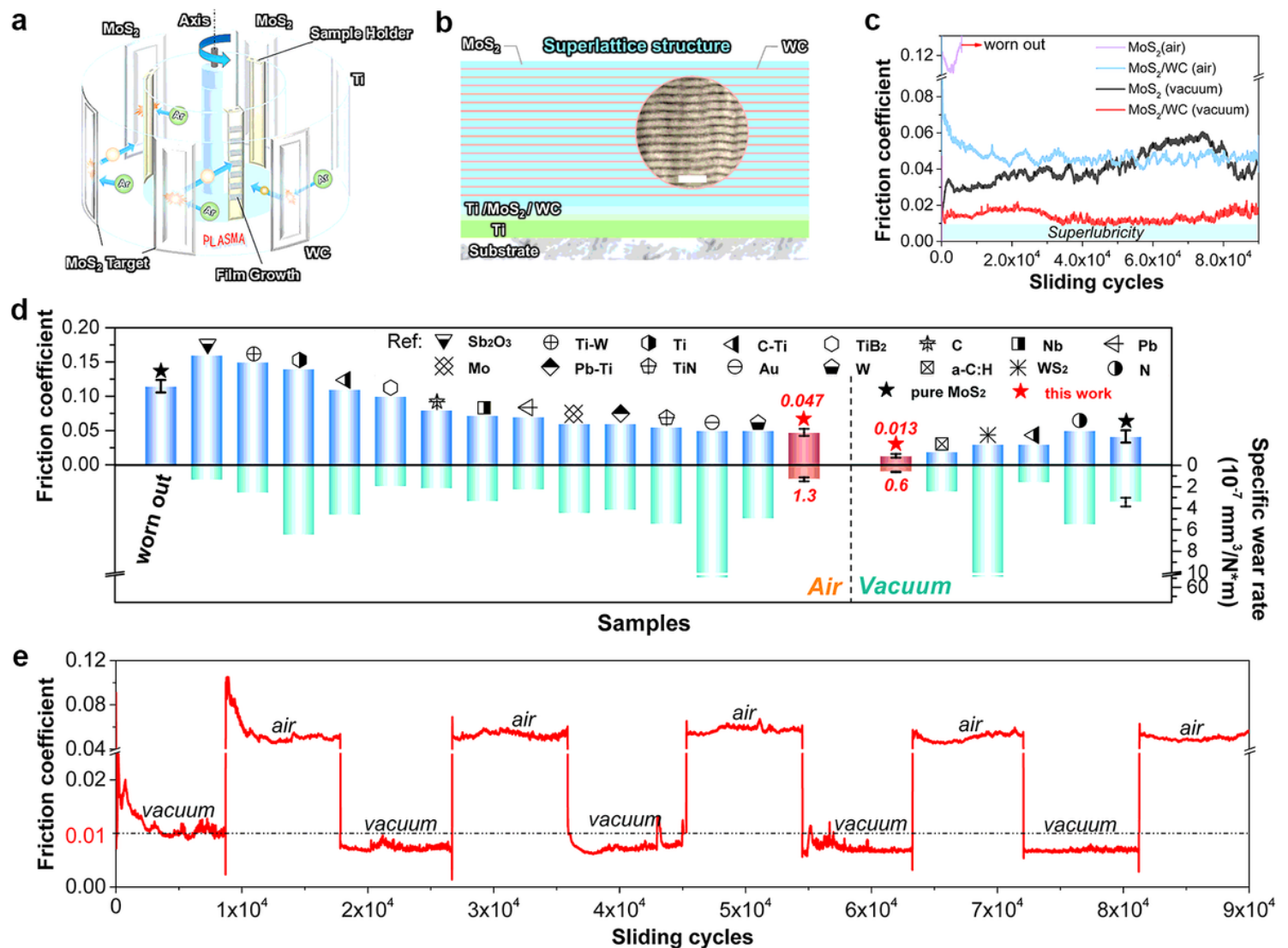


Figure 1

Film growth and tribological behavior of MoS₂/WC superlattice film. **a** Schematic of the experimental design for film growth. **b** Schematic showing the structure of the superlattice film. The inset shows a TEM image of the MoS₂/WC bilayer unit. Scale bar is 30 nm. **c** Friction curves for a pure MoS₂ film and the MoS₂/WC superlattice film in vacuum and air. **d** Average friction coefficient and specific wear rate of various MoS₂-based materials reported in literature (detailed references are in Supplementary Table 2). **e** Friction curves for the MoS₂/WC superlattice film in an alternating vacuum-air environment, where an alternating environmental cycle consists of 9,000 sliding cycles in vacuum and 9,000 sliding cycles in air.

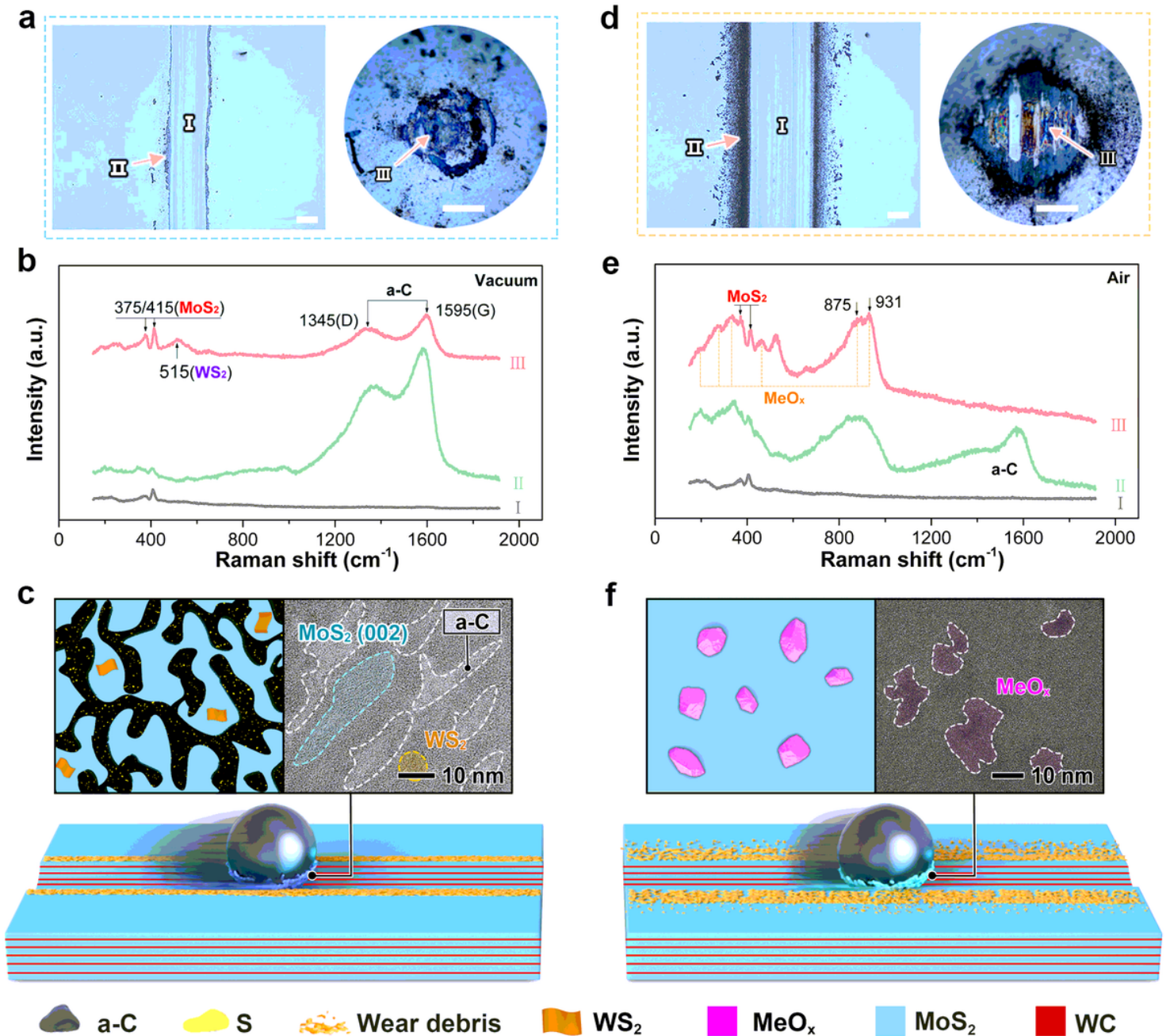


Figure 2

Examinations of the sliding interfaces after tests in vacuum or in humid air. a, d Optical images of the film wear tracks and the ball wear scars for the MoS₂/WC-steel rubbing system after 90,000 sliding cycles in (a) vacuum and (d) air with RH 40%. Scale bars are 100 μm. **b, e** Raman spectra collected from the points identified on the wear tracks and scars after testing in (b) vacuum and (e) air with RH 40%. **c, f** Schematic of the sliding interface in (c) vacuum and (f) air environments. Inset HRTEM images show cross-sectional morphologies of the corresponding tribofilms.

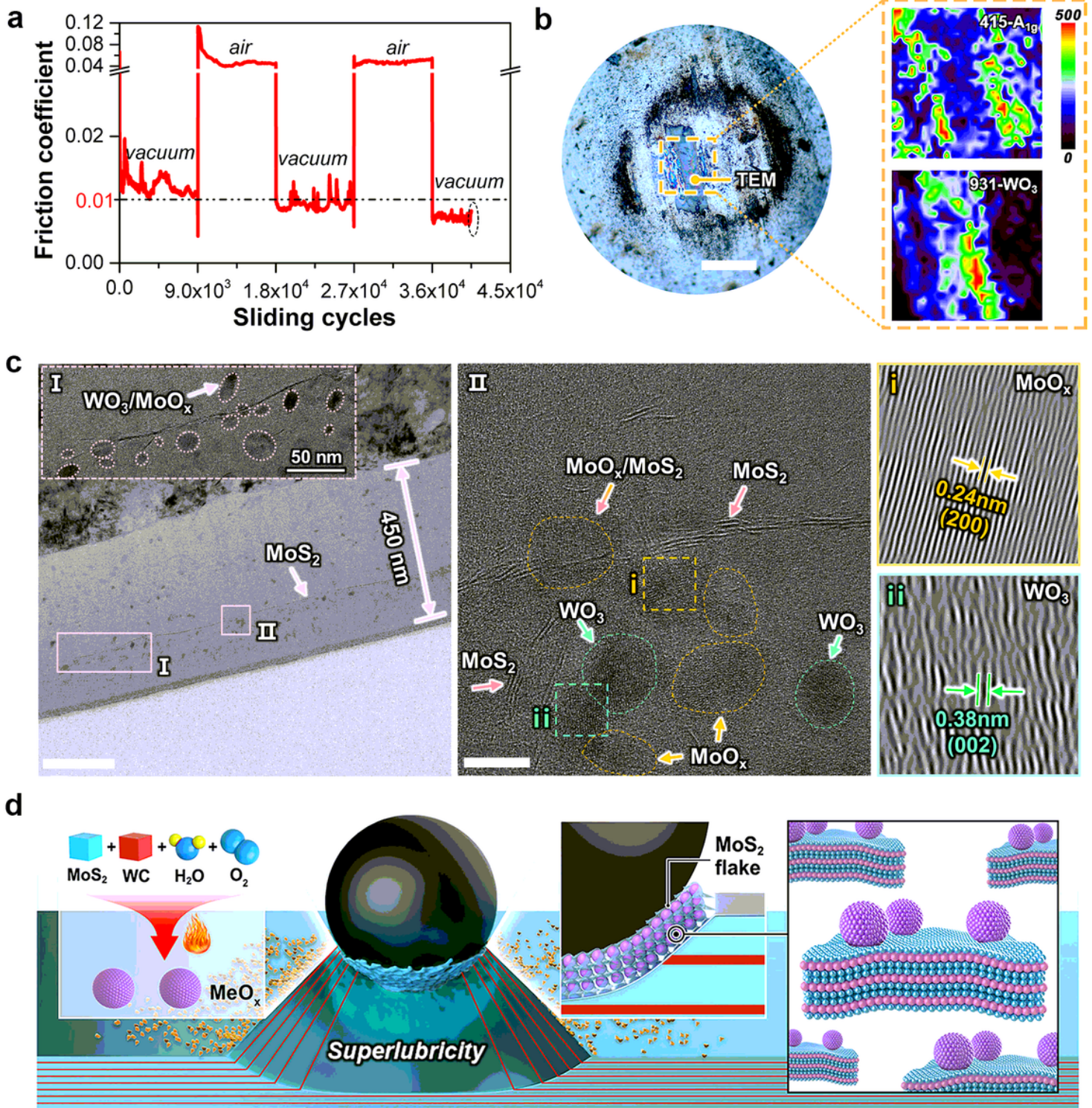


Figure 3

Examinations of the sliding interface when achieving macroscale superlubricity in alternating vacuum-air environment. **a** Friction curve for the MoS₂/WC superlattice film in alternating vacuum-air environment, where the test was interrupted during the third environmental cycle. **b** Optical image of the wear scar when friction test was interrupted. Scale bar is 100 μm. Raman intensity maps of MoS₂-A_{1g} (~415 cm⁻¹) and WO₃ (~931 cm⁻¹) peaks measured in the marked orange rectangle region. **c** TEM and HRTEM images showing the cross-sectional morphology of tribofilm identified on the wear scar (left and middle panel). Scale bars in TEM and HRTEM are 200 nm and 10 nm, respectively. Typical Fourier filtered images of the MeO_x nanoparticles (right panel). **d** Schematic showing the superlubricity mechanisms for the MoS₂/WC-steel system in alternating environment.

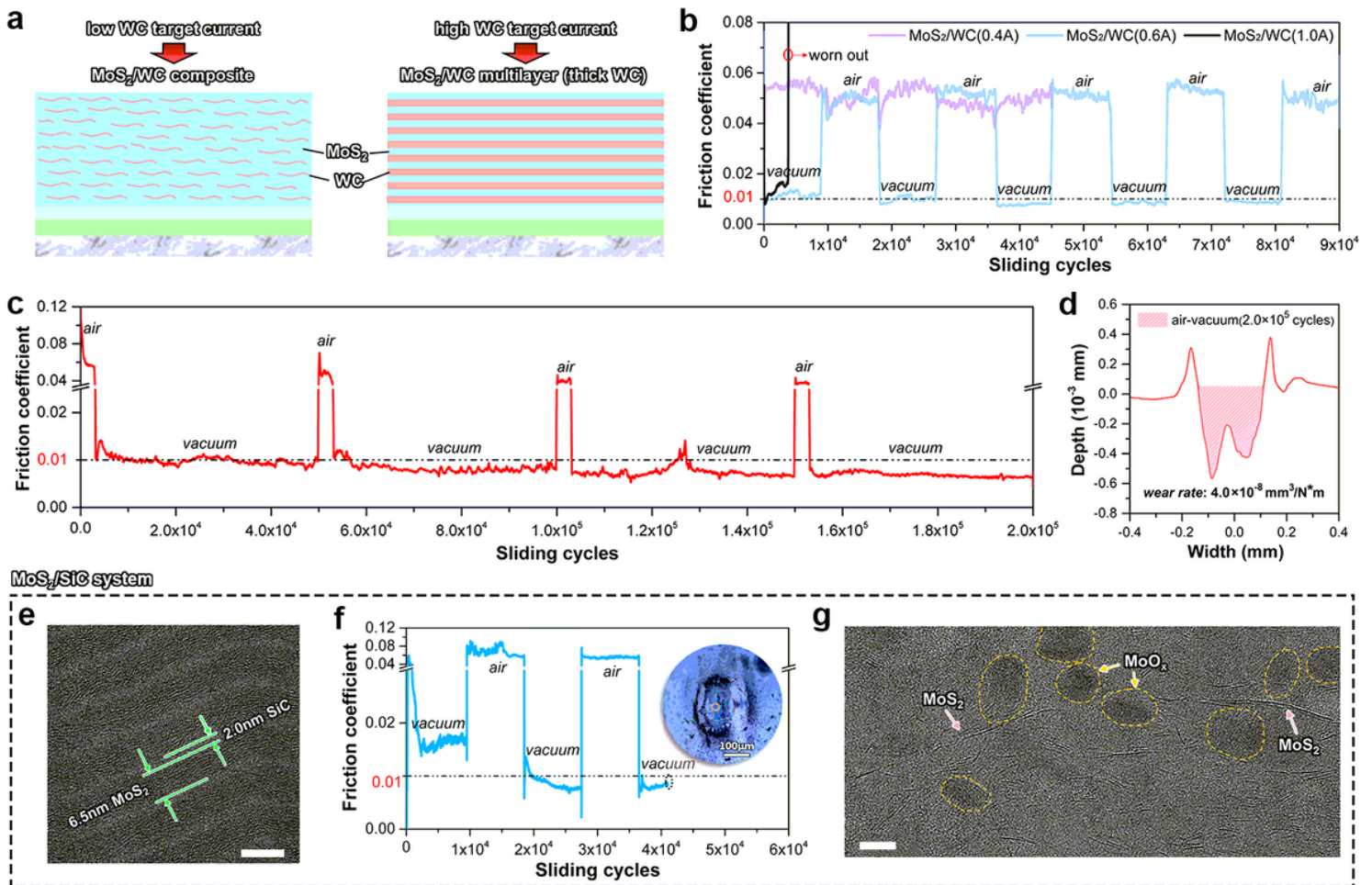


Figure 4

Tribological behaviors of various MoS₂/carbide superlattice films. **a** Schematic of MoS₂/WC composite (left) and multilayer (right) structures deposited with overly low and high WC target current, respectively. **b** Friction curves of MoS₂/WC films with different WC target current slid against steel balls in alternating vacuum-air environment. **c** Friction curve of the optimized MoS₂/WC superlattice film, where the alternating period is 3,000 sliding cycles in air and 47,000 sliding cycles in vacuum. **d** Surface profile of the MoS₂/WC superlattice film after 200,000 sliding cycles in alternating air-vacuum environment. **e**

HRTEM image of the MoS₂/SiC superlattice structure. Scale bar is 10 nm. **f** Friction curve of the MoS₂/SiC film in alternating vacuum-air environment. Inset shows an optical image of the wear scar after test. **g** HRTEM image showing the cross-sectional morphology of tribofilm identified on the wear scar in **(f)**. Scale bar is 10 nm.

Supplementary Files

This is a list of supplementary files associated with this preprint. Click to download.

- [SupplementaryInformation.docx](#)